Brain Topography (2019) 32:215–228
https://doi.org/10.1007/s10548-018-00694-5

ORIGINAL PAPER

Cortical Signal Suppression (CSS) for Detection of Subcortical Activity Using MEG and EEG

John G. Samuelsson[1,2,3] · Sheraz Khan[2,3] · Padmavathi Sundaram[2,3] · Noam Peled[2,3] · Matti S. Hämäläinen[2,3]

Received: 15 May 2018 / Accepted: 17 December 2018 / Published online: 3 January 2019

Abstract

Magnetoencephalography (MEG) and electroencephalography (EEG) use non-invasive sensors to detect neural currents. Since the contribution of superficial neural sources to the measured M/EEG signals are orders-of-magnitude stronger than the contribution of subcortical sources, most MEG and EEG studies have focused on cortical activity. Subcortical structures, however, are centrally involved in both healthy brain function as well as in many neurological disorders such as Alzheimer's disease and Parkinson's disease. In this paper, we present a method that can separate and suppress the cortical signals while preserving the subcortical contributions to the M/EEG data. The resulting signal subspace of the data mainly originates from subcortical structures. Our method works by utilizing short-baseline planar gradiometers with short-sighted sensitivity distributions as reference sensors for cortical activity. Since the method is completely data-driven, forward and inverse modeling are not required. In this study, we use simulations and auditory steady state response experiments in a human subject to demonstrate that the method can remove the cortical signals while sparing the subcortical signals. We also test our method on MEG data recorded in an essential tremor patient with a deep brain stimulation implant and show how it can be used to reduce the DBS artifact in the MEG data by ~99.9% without affecting low frequency brain rhythms.

Keywords Magnetoencephalography · Electroencephalography · Signal processing · Subcortical imaging · Spatial filtering · Temporal subspace projection

Introduction

Deep brain structures are involved in healthy brain function and play critical roles in several neurological disorders such as Alzheimer's disease (hippocampal complex) and Parkinson's disease (basal ganglia) (Obeso et al. 2008; Wanderah and Gould 2016). Functional imaging methods like blood oxygenation level dependent functional MRI (BOLD fMRI) map brain activity in all parts of the brain with good spatial resolution but their temporal resolution is on the order of seconds as they image neuronal activity indirectly via slow hemodynamic changes (Kwong et al. 1992; Ogawa et al. 1990). In comparison, magnetoencephalography (MEG) and electroencephalography (EEG) observe neuronal activity directly with an excellent millisecond-scale temporal resolution (Hämäläinen et al. 1993). Currently, M/EEG are mainly used to estimate distributions of current sources in the cerebral cortex. One reason for this limitation is that M/EEG sensors are located on or outside the head; the sensors being in close proximity to cortical neural signal sources but far away from subcortical sources. M/EEG signals from subcortical structures are therefore typically 1–2 orders of magnitude weaker than those coming from the cerebral cortex (Attal and Schwartz 2013). The signals from superficially located cortical sources are particularly prominent in MEG short-baseline planar gradiometers which detect magnetic field gradients and are less sensitive to deeper subcortical brain sources. In contrast, magnetometers and EEG electrodes have more extended sensitivity distributions (Goldenholz et al. 2009; Hunold et al. 2016) and would be able to detect activity

Handling Editor: Christoph M. Michel.

✉ John G. Samuelsson
johnsam@mit.edu

[1] Harvard-MIT Division of Health Sciences and Technology (HST), Massachusetts Institute of Technology (MIT), Cambridge, MA 02139, USA

[2] Athinoula A. Martinos Center for Biomedical Imaging, Massachusetts General Hospital, Charlestown, MA 02129, USA

[3] Harvard Medical School, Boston, MA 02115, USA

originating in deep structures with a higher signal-to-noise ratio (SNR) in the absence of superficial sources (Ahlfors et al. 2010). In this paper we present a method, Cortical Signal Suppression (CSS), that uses the differences in sensitivity distribution between magnetometers and gradiometers to separate cortical from subcortical activity without forward modeling or source reconstruction. Our method then suppresses cortical contributions to the M/EEG data, revealing activity from subcortical sources. A GitHub repository with the CSS algorithm and code to generate all figures based on simulated data can be found in the following URL: https://github.com/johnsam7/Cortical-Signal-Suppression-CSS.

To validate the efficacy and usefulness of our method, we tested it using simulations, auditory steady state responses (ASSR), and resting-state data collected from an essential tremor (ET) patient with a deep brain stimulation (DBS) implant turned on and off.

Methods

The amplitude of the magnetic field from a primary current dipole source is inversely proportional to the distance squared while the gradient of the magnetic field is inversely proportional to the distance cubed as per Ampère–Laplace's law (Griffiths 2005):

$$\boldsymbol{B}(\boldsymbol{r}) = \frac{\mu_0}{4\pi} \int \frac{\boldsymbol{J}(\boldsymbol{r'}) \times \boldsymbol{R}}{|\boldsymbol{R}|^3} dv'$$

where μ_0 is the magnetic permeability in vacuum, $\boldsymbol{J}$ is the current density, $\boldsymbol{r}$ is the position of the measurement point, $\boldsymbol{r'}$ is the position of the field-generating current and $\boldsymbol{R} = \boldsymbol{r} - \boldsymbol{r'}$ is the vector from the current source to the measurement point. This spatial dependency makes the sensitivity of short-baseline planar gradiometers, which record the gradient of the magnetic field, fall off more quickly with distance than that of magnetometers (Vrba et al. 1982). The Elekta Vectorview MEG system has 102 sensor triplets consisting of one magnetometer and two orthogonal planar gradiometers placed around the head. In this setup, the array of gradiometers is mostly sensitive to cortical sources closest to the sensors while magnetometers are sensitive to distant sources as well. Axial gradiometers used in many MEG systems have two oppositely wound pick-up coils placed in the direction normal to the head surface and is therefore sensitive to the magnetic field gradient in the normal direction. A cortex-covering array of these axial gradiometers has a more extended sensitivity distribution than short-baseline planar gradiometers but less extended than magnetometers (Knuutila et al. 1993). Sensitivity distributions of magnetometers, planar gradiometers and EEG are shown in Fig. 1. EEG electrodes are more sensitive to deep sources than magnetometers because the magnetic field is attenuated due to the spherical symmetry of the head as the source gets closer to the center (Malmivuo et al. 1997). In this work, we used the gradiometers as reference sensors for cortical activity and investigated how the differences in sensitivity distribution between gradiometers and magnetometers/EEG electrodes could be used to suppress the cortical contribution to the magnetometers/EEG signal.

Below, we first describe our CSS method. We then explain the simulations used to validate and assess the efficiency of the method followed by the experimental setup of ASSR experiments. Finally, we describe the experimental setup for recording MEG data from an ET patient with the DBS on and off.

CSS Method Theory

Let M denote the $n_m \times n_t$ magnetometer data matrix and G denote the $n_g \times n_t$ gradiometer data matrix, where n_t is the

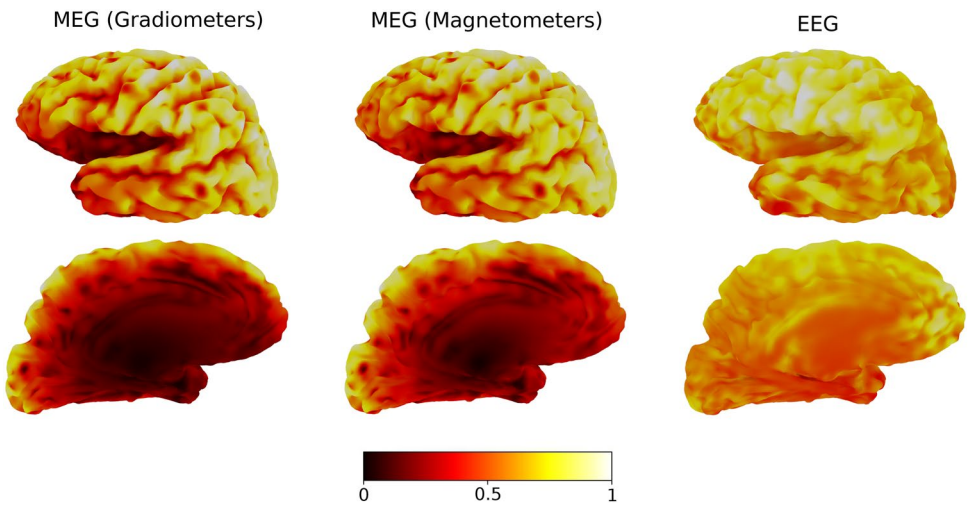

Fig. 1 Sensitivity distributions of MEG and EEG. The figure shows the Euclidean norm of the MEG and EEG sensor array outputs from unit dipoles placed orthogonally to the surface of the left cerebral hemisphere. The values in each column of the figure were separately normalized so that the maximum value over the cortex equals one. The brain surfaces have been partly inflated for illustrative purposes

number of time points, n_m the number of magnetometer channels, and n_g the number of gradiometer channels. There are usually many more time points than measurement channels, i.e., the data matrices are wide ($n_t \gg n_g, n_m$). Let M_c denote the cortical signal in the magnetometers, M_d denote the subcortical signal in the magnetometers, and G_c denote the cortical signal in the gradiometers. Finally, let M_N and G_N be the additive noise in the magnetometers and gradiometers, respectively. Note that because M_c and G_c represent the unknown cortical signals in the magnetometer and gradiometer sensor space, respectively, they will not be the same. As discussed by Ahonen et al. (1993), M and G are linearly related:

$$M \approx AG, \tag{1}$$

where A is a constant matrix of size $n_m \times n_g$. Because $n_t > n_g$, we can find an estimate of A via a least squares fit:

$$\hat{A} = MG^T\left(GG^T\right)^{-1}, \tag{2}$$

where G^T denotes the transpose of G. Because the magnetometers can detect both the subcortical and the cortical signal, while the gradiometers mostly detect the cortical signal, we have,

$$M = M_d + M_c + M_N, \tag{3}$$

$$G \approx G_c + G_N. \tag{4}$$

Rearranging Eq. (3) we get,

$$M_d = M - M_c - M_N. \tag{5}$$

If SNR is much greater than one, then $M_c \gg M_N$ and $G_c \gg G_N$. One can also assume that the cortical signal is much greater than the subcortical signal, so that $M_c \gg M_d$, and it follows then from Eqs. (3) and (4) that

$$M \approx M_c \tag{6}$$

and

$$G \approx G_c. \tag{7}$$

Using Eqs. (6) and (7) in Eq. (1), we get,

$$M_c \approx AG_c. \tag{8}$$

Using Eqs. (7) and (8), Eq. (5) can be written as

$$M_d \approx M - AG. \tag{9}$$

We can now estimate the subcortical signal $\hat{S}_d$ in the sensor space from Eq. (9) using the approximation of A from Eq. (2) as

$$\hat{S}_d = M_d \approx M - MG^T\left(GG^T\right)^{-1}G \tag{10}$$

$$\hat{S}_d = M\left(I - G^T\left(GG^T\right)^{-1}G\right). \tag{11}$$

In Eq. (11), we remove the common temporal subspace between the gradiometers and magnetometers from the magnetometer data, thus suppressing the cortical contribution to the magnetometer measurements. However, subcortical signals are also present in the gradiometer data, albeit of small amplitude. This approach, therefore, risks heavy dampening of the subcortical signal as well. To avoid this dampening effect, we have developed an alternate method in which the dimension of the common subspace to be removed is selectable. Instead of projecting away the entire subspace spanned by the gradiometer data, we only remove a subset of dimensionality r. The subset of the magnetometer data that has the smallest subspace angle (i.e., highest correlation) with the gradiometer data is the subset that is removed. We remove this subset by finding the weighted sums of gradiometer channels that are most correlated with the magnetometer data. The r vectors with the highest correlation are then projected out from the magnetometer data. These r vectors will be referred to as "projection vectors" and following is a detailed derivation of this method, which is the method we call Cortical Signal Suppression, abbreviated CSS. Figure 2 shows the pseudocode of CSS.

Let $U_r = B_r\hat{G}$ be the $r \times n_t$ matrix where the rows are the projection vectors to be removed from the magnetometer data and B_r be a $r \times n_g$ truncated basis change transformation matrix, where each row represents a weighted average of the orthonormalized gradiometer data $\hat{G}$. We are looking for linear transformation matrices B, F for the orthonormalized gradiometer data $\hat{G}$ and magnetometer data $\hat{M}$, respectively, that maximize the correlation between the two data sets. The first row in $B\left(B_{1,:}\right)$ contains the weights of gradiometer

$$\begin{aligned}
\hat{G} &= \text{span}\{G\} \\
\hat{M} &= \text{span}\{M\} \\
C_{gm} &= \hat{G}\hat{M}^T \\
YSZ^T &= C_{gm} \\
U &= Y^T\hat{G} \\
U_r &= U_{(1:r,:)} \\
\hat{S}_d &= M(I - U_r^T U_r)
\end{aligned}$$

Fig. 2 Pseudocode for CSS. G are the gradiometer data and M are the magnetometer data. The span operator orthonormalizes the rows of the data matrices G and M, and transforms them into $\hat{G}$ and $\hat{M}$ where each row is normalized and orthogonal to each other. C_{gm} is the cross-correlation matrix between the orthonormalized gradiometer and magnetometer data. The columns of Y and Z are the left- and right-singular vectors of C_{gm}, respectively, and S the matrix containing the singular values. U are the gradiometer data represented in a new basis and U_r are the first r rows of U. $\hat{S}_d$ is the estimate of subcortical sensor space signal based on the magnetometer data. See Fig. 9 in the Appendix for a graphic illustration of CSS

channels that give the highest correlation with the weighted sum of magnetometer channels $F_{1,:}\hat{M}$:

$$\left(B_{1,:},\ F_{1,:}\right) = \underset{(X,Y)}{\arg\max}\left(X\hat{G}\left(Y\hat{M}\right)^T\right).$$

The second rows in B and F, i.e., $B_{2,:}$ and $F_{2,:}$, are the weighted sums of gradiometers and magnetometers, respectively, that give the highest correlation while being orthogonal to the first row:

$$\left(B_{2,:}\ ,\ F_{2,:}\right) = \underset{(X,Y)}{\arg\max}\left(X\hat{G}\left(Y\hat{M}\right)^T\right),\ s.t.\ X\perp B_{1,:}\ \text{and}\ Y\perp F_{1,:}.$$

For the k:th row, the expression becomes

$$\begin{aligned}\left(B_{k,:},F_{k,:}\right) &= \underset{(X,Y)}{\arg\max}\left(X\hat{G}\left(Y\hat{M}\right)^T\right),\ s.t.\ X\perp\left\{B_{i,:}\right\}_{i=1,\ldots,k-1}\ \text{and}\ Y\perp\left\{F_{i,:}\right\}_{i=1,\ldots,k-1}\\ &= \underset{(X,Y)}{\arg\max}\left(XCY^T\right),\ s.t.\ X\perp\left\{B_{i,:}\right\}_{i=1,\ldots,k-1}\ \text{and}\ Y\perp\left\{F_{i,:}\right\}_{i=1,\ldots,k-1}\end{aligned} \tag{12}$$

where $C = \hat{G}\hat{M}^T$ is the cross-correlation matrix between the gradiometer and magnetometer data. Note that C here is not a symmetric matrix. If we now consider the singular value decomposition (SVD) of $C = RSP^T$, we have that

$$S = R^T CP,$$

since R and P are both unitary matrices, so that $R^TR = I$ and $P^TP = I$. The columns of R and P are the left- and right-sided singular vectors of C, respectively. The SVD chooses the columns of R and P so that the diagonal elements in S are arranged in a descending order while keeping the columns orthogonal. By comparison to Eq. (12), we see that $R = B^T$ and $P = F^T$, so that the left and right singular vectors of C are exactly the weighted sums of gradiometer and magnetometer channels, respectively, that optimize the correlation, given by the singular values $\left\{s_i\right\}_i = \text{diag}(S)$. Thus the projection vectors $U_r = B_r\hat{G}$ can be found by a standard principal angle procedure (Jordan 1875) where we first correlate the orthonormalized magnetometer data $\hat{M}$ with the orthonormalized gradiometer data $\hat{G}$:

$$C_{gm} = \hat{G}\hat{M}^T.$$

The cross-correlation matrix C_{gm} is then factorized using a singular value decomposition,

$$C_{gm} = YSZ^T,$$

and U is finally found by going back to temporal space using the weighted average of the gradiometer data $\hat{G}$ given by the columns of Y;

$$U = Y^T\hat{G}.$$

The singular values are the correlations between the normalized magnetometer data $\hat{M}$ and gradiometer data $\hat{G}$. The principal angles are the cosines of the singular values. Matrices Y and Z are the linear basis transformation matrices, or weighted averages, for the gradiometer and magnetometer data, respectively. The top r rows in U span the subspace of the gradiometer data that has the highest correlation with the magnetometer data. These r vectors are the projection vectors that we will remove from the magnetometer or EEG data instead of the whole gradiometer space G as in Eq. (11);

$$\hat{S}_d = M\left(I - U_r^T\left(U_rU_r^T\right)^{-1}U_r\right) = M\left(I - U_r^TU_r\right), \tag{13}$$

because $U_rU_r^T = I$. Our hypothesis is that the cortical signal lies in the common signal subspace spanned by the most correlated gradiometer and magnetometer signals. Thus the cortical signal can be suppressed by removing this part of the signal subspace. The subcortical signal should be largely unaffected by this operation since it is mainly restricted to the magnetometers or EEG, thus resulting in a selective suppression of the cortical signal. A benefit with this approach is that the dimensionality of the common temporal subspace to be removed r can be tuned for optimal cortical signal suppression and minimal dampening of subcortical signal in different scenarios. This method works best in realistic SNR situations. The pseudocode for our CSS algorithm is shown in Fig. 2.

In cases when SNR is very low, which is often the case in M/EEG experiments, the noise dominates the data to such an extent that the cortical and subcortical signals are overshadowed by noise and get smeared over the common subspace vector elements, resulting in poor performance with CSS. This problem can be addressed by finding the projection vectors U_r based on the epoch-averaged data, and then applying the filter to each epoch individually. That way, the SNR can be increased to an acceptable level before finding the principal vectors and the cortical signals.

Simulations

We performed simulations using the MNE-Python software package (Gramfort et al. 2013). The purpose of the simulations was to demonstrate how the algorithm works under ideal conditions with high SNR, performance during low SNR and how performance varied depending on activated brain areas. We used the "sample" subject provided with the

MNE software for simulations. The simulated MEG signals were assumed to be measured with a 306-channel Vectorview system positioned at the location given by the sample data set. A three-compartment piecewise homogenous conductor model of the head and the boundary-element method (BEM) were used for forward calculations (Mosher et al. 1999). A surface source-space of the cerebral hemispheres with restricted dipole orientations were used to simulate neuronal activity in different brain areas. The added noise was white multivariate Gaussian with spatial structure taken from real sample data covariance.

Auditory Steady-State Responses (ASSR)

Rationale

When an amplitude-modulated (AM) tone with AM-frequency f_{AM} is presented to a human subject, the evoked neural response is phase-locked to the modulation wave form. The amount of neuronal synchronization varies with modulation frequency and peaks at $f_{AM} = 40$ Hz (Hari et al. 1989). The signal strength decays rapidly as the modulation frequency f_{AM} is increased for $f_{AM} > 80$ Hz and plateaus for $f_{AM} > 150$ Hz. The phase-locked signals at $f_{AM} > 150$ Hz arise from subcortical structures in the brainstem, whereas the strong 40-Hz response is dominated by signals coming from the auditory cortex (Kuwada et al. 2002). The brainstem structures in the auditory pathway that generate auditory brainstem responses (ABR) are the cochlear nuclei, superior olivary complex, inferior colliculi and the medial geniculate nuclei of the thalamus (Coffey et al. 2016; Wanderah and Gould 2016). As noted by Kuwada et al. (2002) in their investigation of the amplitude-modulation following response in rabbits using invasive recordings, the modulation transfer function along the auditory pathway can be modeled as a low-pass filter where the cutoff-frequency gets lower ascending the pathway. Utilizing this prior information, we can frequency tag the cortical and subcortical (brainstem) signals using different modulation frequencies. Thus, using a combined amplitude modulation of $f_1 = 40$ Hz and $f_2 = 223$ Hz, we can elicit frequency-tagged activity in the cortex ($f_1 = 40$ Hz) and in a subcortical structure ($f_2 = 223$ Hz) simultaneously. This approach allows us to benchmark our method with real neurophysiology data in the sensor space without having to resort to source estimation.

Procedure

MEG and MRI research data were collected after informed consent from a healthy 27-year old male under a protocol approved by the Massachusetts General Hospital Institutional Review Board. The subject had no medical history of hearing loss. Evoked ASSR were recorded in two different study sessions, the first using only MEG (1200 epochs) and the second using simultaneous MEG-EEG (1653 epochs). The MEG system was an Elekta-Neuromag VectorView (Elekta, Stockholm, Sweden) with 306 channels; 102 triplets of one magnetometer and two orthogonal planar gradiometers. The EEG was recorded with the EEG system integrated with the VectorView machine using a 58-channel MEG-compatible EEG cap (EasyCap GmbH, Germany). The experiment was performed in a quiet, magnetically shielded room (IMEDCO, Switzerland). The recording bandpass filter was 0.1–1650 Hz and the data were digitized at 5000 Hz.

Stimuli

Tones presented to the subject had a carrier frequency of 1000 Hz and were amplitude modulated to a depth of 90% by a superposition of 40 Hz and 223 Hz sinusoids:

$$y(t) = \left(0.1 + \beta[\sin\left(2\pi f_1 t\right) + \sin\left(2\pi f_2 t\right)]/2\right)\sin\left(2\pi f_0 t\right),$$

where $f_0 = 1000$ Hz, $f_1 = 40$ Hz, $f_2 = 223$ Hz, and $\beta = 0.9$. The stimulus duration was 1 s with a random inter-stimulus interval (ISI) evenly distributed between 0.5 and 1.25 s to avoid habituation. The sound stimulus was created in MATLAB 2010b (Mathworks, Natick (MA), US) on a MacBook computer (Apple Inc., Cupertino (CA), US) connected to a speaker system (Unides ADU1b, Helsinki, Finland). The speaker system was placed outside the shielded room and connected via 3.25 m long plastic tubes to foam earpieces placed in the subject's ears. The sound card sample rate for the stimulus was 22,050 Hz and the audio bit depth was 16 bit. The loudness was adjusted to a level that was perceived as comfortable yet clearly audible to the subject. Although the AM waveform in the digital stimulus only had spectral components at $f = 40$ Hz and $f = 223$ Hz, the acoustic signal at the output of the earpieces had a more complex range of modes introduced by mechanical distortions in the tubephones (Fig. 8 in the Appendix). Because the neural response is phase-locked to the acoustic signal that reaches the cochlea, these acoustic modes represented in Fig. 8 were also present in the spectra of the MEG and EEG ASSR signals. This topic is discussed further in the Appendix.

Analysis

To avoid attenuation of signals from subcortical structures, we did not apply signal-space projection (SSP) to the data (Uusitalo and Ilmoniemi 1997). Although some previous studies that have reported auditory brainstem responses (ABR) with MEG did apply SSP, e.g., Parkkonen et al. (2009), we did not do so because it resulted in a net loss of SNR in the raw data as quantified by z-score of phase locking value (PLV) between magnetometer channels and

over duration of ASSR at 223 Hz. This is most likely due to the very low amount of environmental noise in our shielded room. Whether SSP should be applied when studying deep brain structures and how many projection vectors to use must be determined on a case-by-case basis as this depends on the amount of environmental noise and the amplitude of the elicited neural response. We analyzed both the spectral peaks in the response and PLV as a function of frequency (Lachaux et al. 1999). The PLV was calculated through a complex principal component analysis (cPCA) as the first eigenvalue of the normalized cross-spectral density matrix corresponding to each frequency bin separately, according to the procedure presented in Bharadwaj and Shinn-Cunningham (2014). The phases of the entries in the complex-valued first eigenvector are then the optimal phase shifts to each channel.

Deep Brain Stimulation

Rationale

In deep brain stimulation (DBS), the stimulating electrode in the target brain structure is usually connected to control electronics placed near the patient's clavicle via subdermal leads in the head and neck regions (Fitzpatrick et al. 2005). The currents in these leads produce an artifact that is several orders of magnitude higher than neurophysiological signals, thus contaminating M/EEG measurements (Allen et al. 2010). Because the leads are under the skin, the artifact source is close to the M/EEG sensors; in fact, it is closer to some of the sensors than the cerebral cortex is. Since CSS removes signals that emerge from superficial sources close to the sensors, we hypothesized that our method could be used to suppress DBS artifacts as well.

Procedure

Institutional Review Board approval was obtained for MEG studies in ET patients with implanted DBS. Written consent was obtained from the patient prior to the study. One ET patient (58-year-old male) was recruited for our study. The patient had DBS electrodes (Medtronic, Minneapolis, USA, Model 3387) stereotactically placed on the patient's left side in the posterior part of the ventrolateral thalamus (VLp), also known as the ventral intermediate nucleus (Vim). The implanted DBS electrode was 1.27 mm in diameter and had a 10.5 mm extent with four electrodes (1.5 mm inter-electrode spacing) at the distal end while the proximal end was fitted into a four-conductor connector that was connected to the neurostimulator (Medtronic, Minneapolis, USA) located subcutaneously in the subclavicular region.

MEG data were acquired inside a magnetically shielded room using an Elekta Neuromag VectorView system composed of 306 sensors arranged in 102 triplets of two orthogonal planar gradiometers (204 total) and one magnetometer (102 total). The signals were band-passed filtered between 0.1 and 330 Hz and sampled at 1000 Hz.

Two 6-min long resting-state recordings were used in this study. For the first recording, the subject was instructed to stay still and relaxed with his eyes open, and the DBS stimulator was on at standard clinical settings. For the second recording, the subject was instructed to turn off the neurostimulator and once again remain still with his eyes open.

Results

Simulations

High SNR

To test the efficacy of the method under ideal conditions, one cortical patch around the central sulcus and one subcortical patch in the para-hippocampal area were activated with uniform distributions of dipoles oriented normal to the patch surfaces. The amplitude of the dipoles in the cortical and subcortical patches varied sinusoidally at 40 Hz and 223 Hz, respectively, with an SNR of 120 dB. The synthetic data were processed with CSS, using one projection vector ($r = 1$). To examine the effect of processing on the subcortical and cortical signals separately, the raw and processed data were divided into cortical and subcortical components by using a low-pass and high-pass 5th order Butterworth filter, respectively, with cutoff frequency $\omega_c = 100$ Hz. The results of these simulations are displayed in Fig. 3 which shows the time signal and spectral density of channel MEG1631 located in the left-superior-posterior quadrant of the helmet, a few centimeters behind the left ear. CSS almost completely removed (~99%) the cortical component of the signal while preserving the subcortical signal without introducing any phase distortion.

Low SNR

Simulation results for SNR = 0.5 dB are shown in Fig. 4. Unlike for higher SNR, when the signal was dominated by only two orthogonal signals (in L_2-inner product space meaning), the spectral characteristics of the signal are more complicated because of the noise. This noise contamination makes it less likely for the correlation between gradiometers and magnetometers to lock onto the cortical signal, and the cortical and subcortical signals smear out over the common temporal subspace vectors U as a result, making an adequate selection of the number of projection vectors r critical. This is illustrated in Fig. 4, which shows how the cortical signal power (P_{cort}) and subcortical signal power

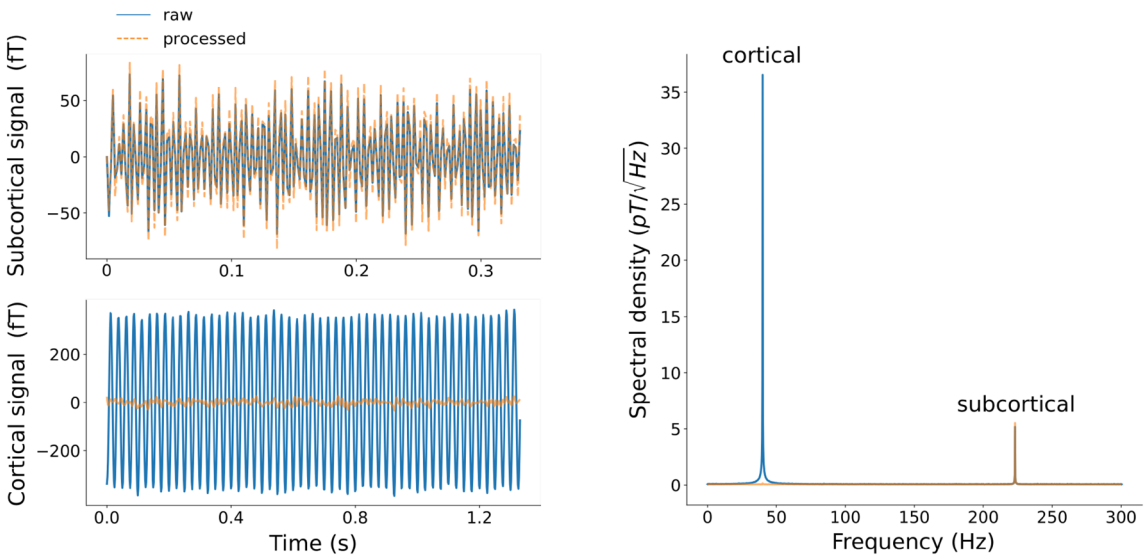

Fig. 3 High SNR simulations (SNR = 120 dB) of one activated cortical patch around the central sulcus (f = 40 Hz) and one subcortical patch in the para-hippocampal area (f = 223 Hz) processed with CSS. Raw and processed time signals of subcortical and cortical signals with r = 1 and their spectral density

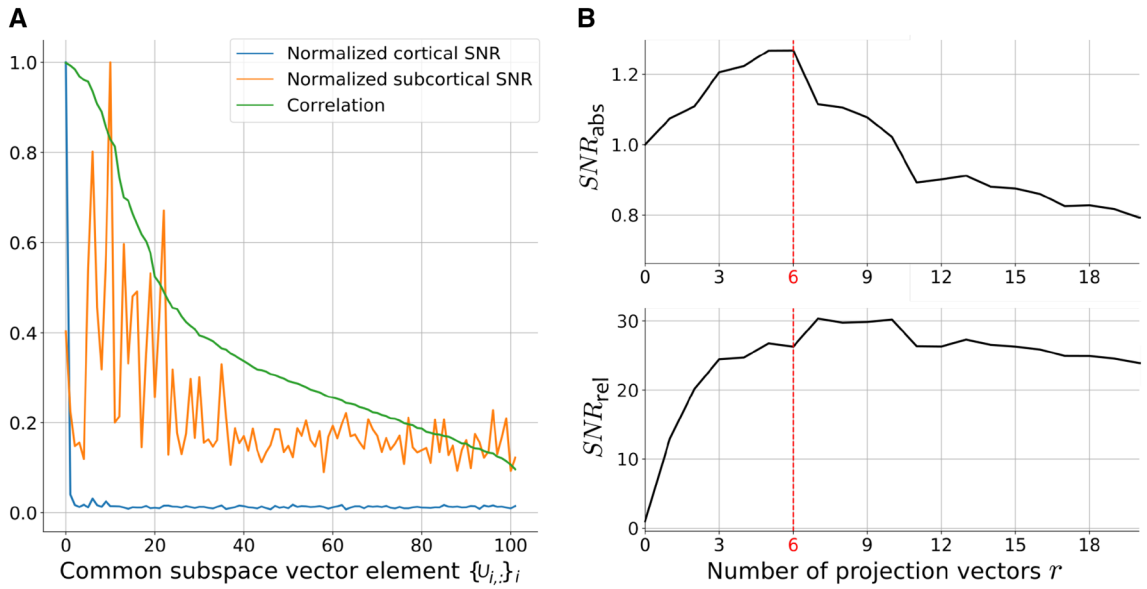

Fig. 4 Low SNR simulations (SNR = 0.5 dB) of one cortical neural patch around the central sulcus (f = 40 Hz) and one subcortical patch in the parahippocampal area (f = 223 Hz). **a** Normalized cortical and subcortical SNR and correlation between the gradiometers and magnetometers for different common subspace vector elements $U_{i,:}$. **b** Absolute and relative SNR change caused by processing of data with CSS as a function of number of projection vectors (r) (top and bottom, respectively)

(P_{subcort}) are distributed over the common subspace elements (Fig. 4a). Figure 4b shows how the absolute- and relative SNR, defined as

$$SNR_{\text{abs}} = P_{\text{subcort}}/P_{\text{tot}},$$

$$SNR_{\text{rel}} = P_{\text{subcort}}/P_{\text{cort}},$$

change as a function of the number of projection vectors r. The cortical component is mainly in the first common subspace element that represents the highest correlation between the gradiometers and magnetometers. The subcortical component is more complex and appears in the common subspace vector elements 5–20, as ranked by correlation. According to these data, one should expect the optimal

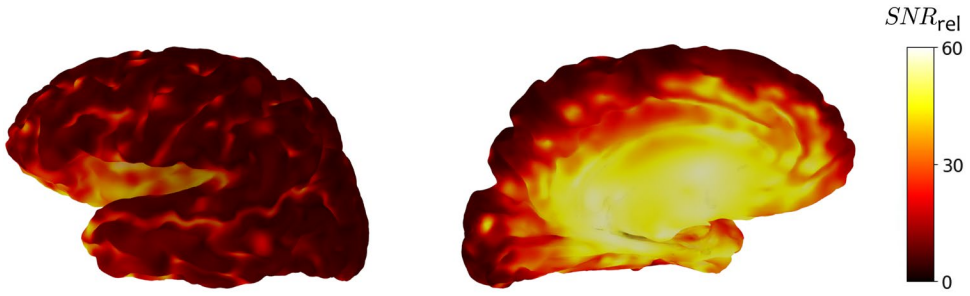

Fig. 5 Simulations showing the relative SNR change after processing with CSS as a function of location over the left cerebral hemisphere. Synthetic data had an original SNR of 0.5 dB and number of projection vectors $r = 6$

subcortical SNR increase to be in the range of $r \sim 1 - 7$. Figure 4b shows that the peak in absolute SNR change $\left(\frac{SNR_{\text{abs proc}}}{SNR_{\text{abs raw.}}}\right)$ is indeed at $r = 6$ and relative SNR change $\left(\frac{SNR_{\text{rel proc}}}{SNR_{\text{rel raw}}}\right)$ at $r = 7$.

To test how the algorithm performed as a function of location of the subcortical signal generator, simulated current dipoles were placed at each vertex of the cerebral hemispheres with fixed orientations and 10 nAm amplitude, varying sinusoidally at 40 Hz with an SNR of 0.5 dB. One of the dipoles, representing "subcortical" activity, then had its waveform changed to an amplitude of 100 nAm varying at 223 Hz and the MEG signal was simulated for this current configuration and processed with CSS using six projection vectors ($r = 6$), as was previously shown to be an appropriate number as a rule of thumb. This process was repeated for each dipole, so that each dipole had its waveform changed to 223 Hz in one simulation. The relative SNR change was then plotted at the location of the 223 Hz dipole representing the "subcortical" source and the results are shown in Fig. 5. As expected, the relative SNR change was lowest in the cortical regions and highest in the deep sulci and subcortical regions, reaching as high as 60 in the area around the thalamus.

ASSR Experiments

ASSR data were processed with CSS. The MEG magnetometer data were processed according to the CSS pseudocode in Fig. 2, where the epoch average was used as input gradiometer data G and input magnetometer data M to create the projection vectors U_r. Each epoch of magnetometer data was then processed individually by U_r. The same projection vectors U_r were then also used to process the EEG epochs; the filter was thus constructed using the averages of MEG magnetometers and gradiometers and then applied to each epoch of EEG and magnetometer data individually. All steps in the processing of EEG data were thus the same as when processing the magnetometer data, up to the last projection step, as outlined in Fig. 2, where the magnetometer data were exchanged for the EEG data, so that $\widehat{S}_d = E(I - U_r^T U_r)$, where E is the EEG data matrix. The magnetometer data were filtered with three projection vectors ($r = 3$) and EEG data with six projection vectors ($r = 6$). To estimate the reliability of the performance of CSS, bootstrapping was done in 200 trials where 1000 epochs were randomly selected with replacement from the available 1653 epochs of EEG data and 2000 epochs were randomly selected with replacement from the available 2853 epochs of MEG data. These epochs were filtered with CSS and PLV across MEG magnetometers and EEG electrodes were calculated over the duration of each stimuli for each frequency separately. We refer the reader to the Appendix for an explanation of PLV. The results are shown in Fig. 6, which displays the bootstrap distribution of the calculated PLV as a function of frequency for raw and processed magnetometer and EEG data.

Significant peaks in PLV can be seen for frequencies $f = 40, 223, 263$ Hz in the EEG data and for $f = 40, 63, 80, 103, 140, 183, 223, 263$ Hz in the MEG magnetometer data. The strongest time-locked response in both data sets was at $f = 40$ Hz, which represents the cortical signal. Another prominent feature was the response at $f = 223$ Hz, which originates from the subcortex. The origins of most of the other peaks in the spectra can be traced to mechanical distortions in the tubephones that were subsequently transduced into a neural response, as evident from Fig. 8 in the Appendix. An extended discussion on this topic can be found in the Appendix.

The signal in the MEG magnetometer data at $f = 40$ Hz was suppressed by 97% to slightly above the noise floor using CSS, while the subcortical SNR ($f = 223$ Hz) was increased by a factor of 10%, as quantified by PLV (Fig. 6). The 40 Hz signal in the EEG data was suppressed by 75%, while having little effect on the subcortical signal at $f = 223$ Hz. These results imply that the method is efficient in identifying subcortical activity in EEG as well. Note that the filter $(I - U_r^T U_r)$ is constructed from gradiometer and magnetometer data; all MEG channels are therefore employed to construct the EEG data filter.

Deep brain stimulation artifact removal

MEG resting state data from the ET patient with a DBS implant was first filtered with signal subspace projection (SSP) applying four projection vectors based on empty

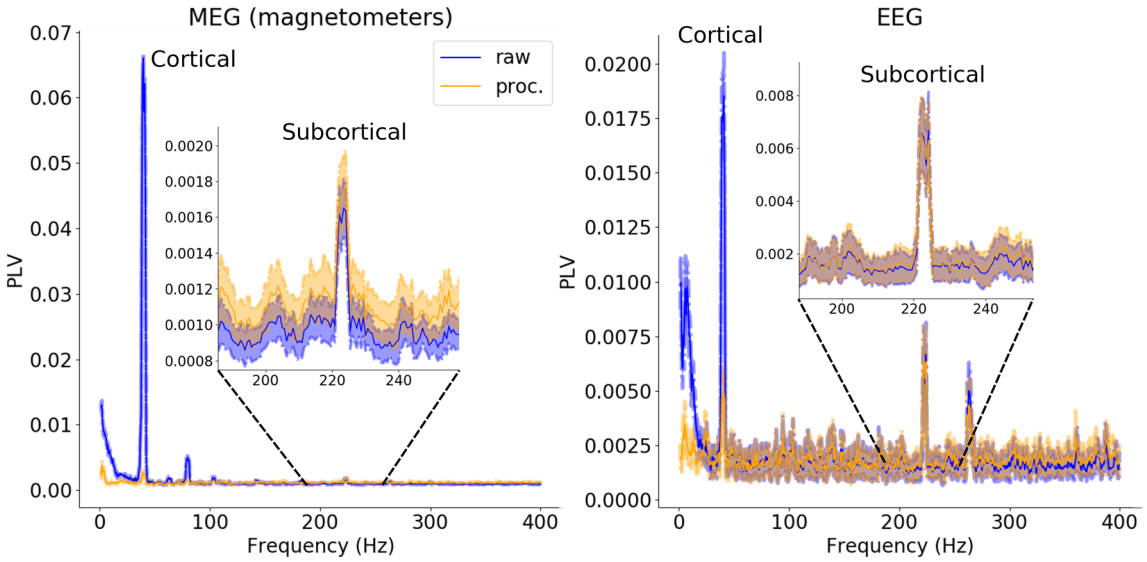

Fig. 6 Bootstrap distribution ($N=200$) of raw (blue) and processed (orange) ASSR data collected from a human subject. The plot shows phase locking value (PLV) between MEG magnetometer channels (left) and EEG channels (right) over duration of stimulus and trials as a function of frequency. The solid line represents the median value and the transparent range plus/minus one standard deviation. The insets show a magnification of the subcortical response at f = 223 Hz

room data. The gradiometer data with DBS on were high-pass filtered using a fifth-order Butterworth filter with a cutoff frequency of $\omega_c = 50$ Hz and the magnetometer data with DBS on were processed with CSS ($r = 6$) using the filtered gradiometer data as input and compared to resting-state data with DBS off. The results are shown in Fig. 7. All three data sets (raw and processed resting state data with DBS turned on and raw resting state data with DBS turned off) were essentially the same for all brain rhythms up to $f = 50$ Hz. For frequencies above $f = 50$ Hz, however, there was a huge stimulation contamination to the MEG signal, as expected. The contamination was biggest around 130 Hz with both subharmonics (multiples of 65 Hz) and harmonics (multiples of 130 Hz). Processing with CSS suppressed peak contamination around the stimulation frequencies (multiples of 130 Hz) by more than 99.9% while preserving all brain rhythms below 50 Hz and just slightly dampening the frequency bands between the stimulation peaks. Because the stimulation harmonics were about four orders of magnitude stronger than physiological data at their peak, the stimulation harmonics

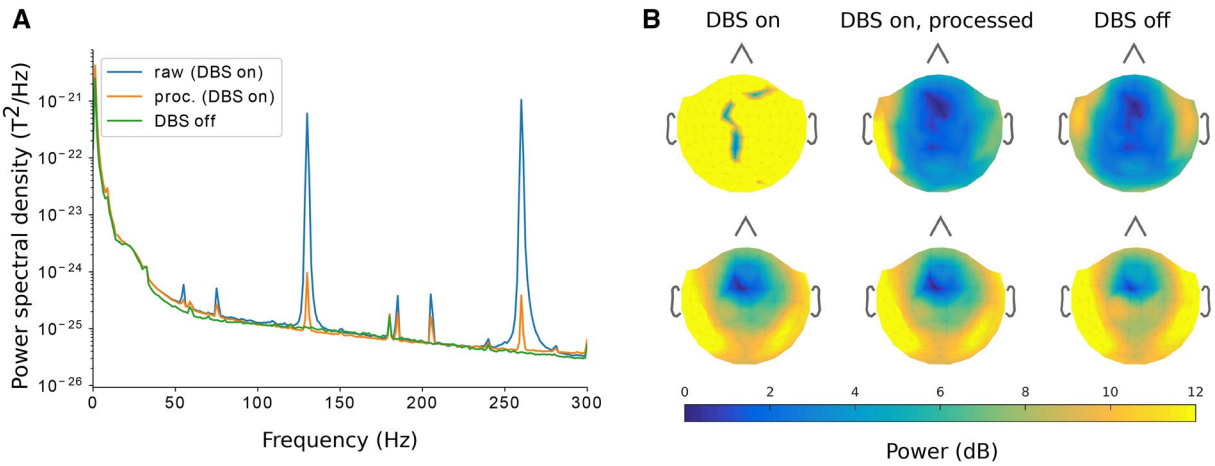

Fig. 7 Processing of resting state data from ET patient with DBS turned on. **a** Logarithmic plot of power spectral density (PSD) of resting state data with DBS on (raw), DBS on after CSS-processing (proc.) and DBS off. **b** Topoplot of magnetometer power distribution of high-pass filtered data ($\omega_c = 50$ Hz) that includes DBS artifacts (upper row) and alpha band (8–12 Hz) (lower row)

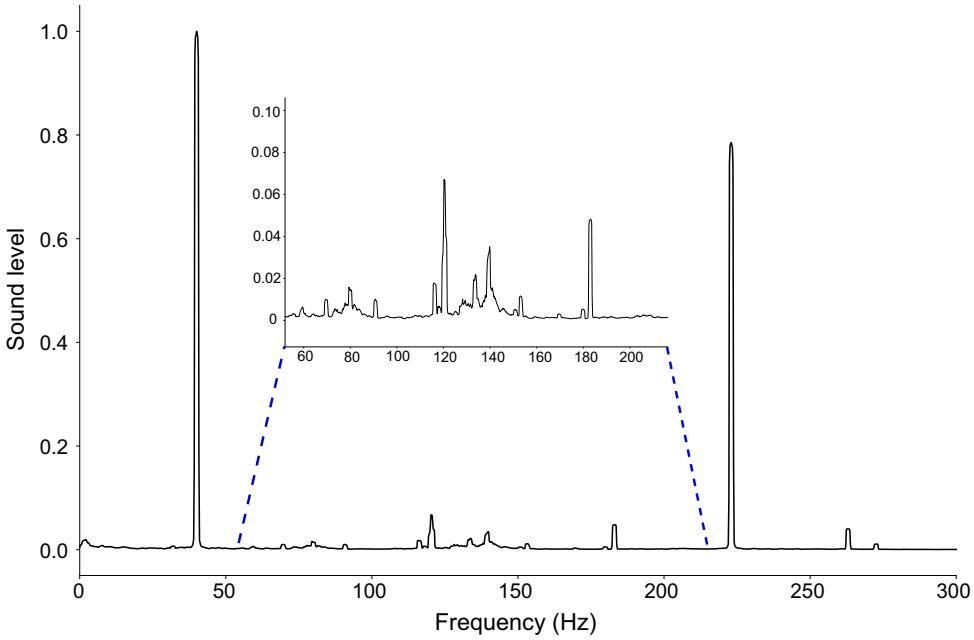

Fig. 8 Power spectral density (PSD) normalized to the peak value at f = 40 Hz of ASSR sound stimulus measured in dB(A). PSD was computed using a multi-taper sequence of Slepian tapers with 5 s time windows and 0.25 overlap fraction

completely dominated the MEG signal in the raw data. When those were dampened by CSS, the spatial distribution of signal power collected with DBS turned off was qualitatively similar to the processed data (Fig. 7b).

Discussion

There is a pressing need for functional imaging methods with sufficient temporal resolution to adequately capture the detailed time course and spatial distribution of subcortical activity. Here we propose a method that suppresses cortical signals and dampens cortical background activity. This leads to greatly increased relative SNR of subcortical activity and may also yield moderate increases in absolute SNR. To test the usefulness of the method, we applied it to human ASSR data. In the case of ASSR, results showed that the method does suppress signals from cortical sources while sparing subcortical signals.

Many contemporary MEG systems employ only axial gradiometers, and there are reports of subcortical activity being recorded with such systems. One example is Coffey et al. (2016) who studied auditory brainstem responses using a system with axial gradiometers. In that study, activity in different brain regions were separated by MNE inverse modeling. Because the underlying principle of CSS relies on two different sets of sensor data, one can only apply CSS in these systems if simultaneous EEG is acquired. The reference sensors for cortical activity would then be the axial gradiometers and the EEG sensors would be used to access subcortical electrophysiology data.

Unlike most previously presented methods that try to separate MEG/EEG signals from different regions, this method does not rely on source estimation. Therefore, this method should be considered complementary to inverse methods or spatial filters that rely on forward models. Initial source modeling is not necessary because the filter is completely data based: information on subject-specific anatomy and electrical conductivity distribution are not necessary. CSS should therefore be used as a first step in the analysis process and viewed as a method for detecting subcortical activity in the sensor space, and not as an alternative to beamformers or other source reconstruction methods. It is also important to note that the temporal projection applied in CSS reduces the signal power in the sensors based on their temporal content. Signal power in sensors close to the primary cortical source will be reduced more than signal power in sensors far away from the cortical source due to the difference in their temporal contents. Compensation would therefore have to be applied to the candidate source waveforms when doing source estimation with CSS-processed data to yield unbiased results.

The underlying principle of CSS is the removal of a shared signal subspace between two datasets, thereby achieving a more focused processed signal which only contains the disjoint spaces of the initial data. We believe that this approach can be extended to other datasets to separate signals other than cortical-subcortical, e.g., to MEG magnetometers and EEG to acquire signals from only radial sources, as these are undetectable in MEG but present in EEG.

Scalp magnetometers, as made possible by recent advances in optically pumped magnetometers (OPM) (Jiménez-Martínez et al. 2012), are about 2 cm closer to the cortex than contemporary magnetometers, making the

cortical signal considerably stronger in the magnetometers but the subcortical signal only moderately stronger. Thus, the problem of cortical signals obscuring subcortical signals may prove to be an even bigger challenge in future MEG systems employing OPM technology. Using OPM in conjunction with contemporary gradiometers or EEG and processing the data with CSS could be an effective way of dealing with this issue and unlocking the full potential of subcortical imaging in next-generation MEG systems.

Limitations

Previous studies that have investigated the neurophysiology of DBS patients with MEG have found that dystonic movements of DBS patients, especially with DBS off, can yield large low-frequency magnetic artifacts arising from the movement of the DBS material itself (Airaksinen et al. 2011). Assessing the full scope of the degree to which CSS can suppress these and other types of artifacts, as well as a systematic comparison between CSS and other artifact suppression methods such as tSSS and Hampel filtering (Allen et al. 2010; Taulu and Hari 2009) should be the topic of a future study. Another potential limitation of CSS lies in processing MEG data of subjects with small-sized heads, e.g., children in adult-sized MEG systems. In this case, the cortical and subcortical sources will be closer to each other in relation to the distance to the sensors and the difference in sensitivity to cortical and subcortical sources between gradiometers and magnetometers will be smaller, making CSS less effective at separating the two.

When neural signals are not orthogonal in time and there is a temporal overlap between cortical and subcortical sources, the dampening of subcortical sources increases. To significantly dampen the subcortical signals, however, the sources need to be at the same frequency and have little phase shift. Although this does not usually happen, it is important to keep in mind as elicited neural responses to sensory stimuli are usually phase-locked between brain regions and to the stimulus. If the stimulus frequency is chosen such that the time lag between subcortical- and cortical regions corresponds to a natural number of periods, then the deep and cortical sources will be of the same frequency and in phase, meaning that the deep sources cannot be separated from the cortical sources based on temporal information. To optimize SNR gain, therefore, it is recommended to keep this fact in mind when designing experiments.

Conclusion

For enhanced detection of subcortical MEG/EEG signals, we presented a method called Cortical Signal Suppression (CSS) that can separate and suppress cortical contributions to the data while preserving contributions from subcortical regions, facilitating their detection and analysis. We demonstrated the efficacy of this method using simulations and human auditory steady-state responses. Application of CSS to MEG magnetometer and EEG data significantly reduced cortical signal strength while sparing the subcortical signal. In resting-state recordings from an essential tremor patient with a deep brain stimulator implant, CSS reduced the stimulation artifact by ~99.9% at the stimulation harmonic peaks without affecting low-frequency brain rhythms. The CSS method is completely data-driven: no MRI, forward modeling or source reconstruction methods are required. CSS is thus particularly useful for detecting signals from deep structures and their initial evaluation in the sensor space.

Acknowledgements This work was supported by the National Institute of Biomedical Imaging and Bioengineering (P41EB015896), the National Institute of Mental Health (R01MH106174) and the Martinos foundation.

Appendix

ASSR

To differentiate signals of acoustic origin in the tubephones from those of neural origin, the sound output at one of the earpieces was measured using a coupler of model G.R.A.S. Sound & Vibration IEC 60126 2 cc (Nærum, Denmark) connected to a sound level meter of model Larson Davis SoundTrack LxT2 (Depew (NY), US). The average loudness was measured to be 83 dB (A), although the sound level in the actual experiment was somewhat lower because the subject expressed discomfort with the loudness and it was subsequently decreased. The power spectral density (PSD) of the acoustic signal was computed using Slepian tapers with 5 s windows and 0.25 overlap fraction between windows and is shown in Fig. 8. There are several spectral peaks of mechanical origin that was not in the stimulus spectrum: 70, 80, 90, 116, 120, 133, 153, 180, 183, 263 and 273 Hz were all not in the digital stimulus signal but present in the acoustic ASSR signal and must therefore be the result of acoustic modes in the tubephones. Some of these peaks are also seen in the neural response (Fig. 6). However, there was no significant acoustic signal power at $f = 63$ and 103 Hz, both of which were prominent in the neural ASSR data. These signals must thus either be of acoustic origin from the ear canal or inner ear, or of neural origin. Tracing the origin of these signals is difficult as it would either require invasive sound measurement or CFD simulations with very exact subject-specific anatomy, because flows through confined channels such as the inner ear have been shown to be extremely sensitive to shape variations (Samuelsson et al. 2015) and is beyond the scope of this paper.

PLV

Phase locking value (PLV) is the vector sum of phase differences between different channels. In our case, we have also included the phase difference at different time points because the neural ASSR is steady throughout the epoch after the initial transients. See Bharadwaj and Shinn-Cunningham (2014) for details on how to calculate PLV. If there is only noise at a particular frequency, there will be no phase locking in the neural response and the phase difference at that frequency will be random, uniformly distributed around the unit circle in the complex plane. In such a case, the magnitude of the average of the phase differences will be close to zero. Because we know that the neural response is phase-locked to the modulation wave form of the auditory stimulus, PLV is a good metric for SNR; a higher PLV implies a stronger neural phase locking response and a higher SNR.

How Does CSS Relate to a Wiener Filter?

Suppose that we have a contaminated signal x and a signal of interest y so that $x = y + n$ where n is noise or some other signal of no interest. One can then filter the signal using a Wiener filter by

$$Y(z) = H(z)X(z),$$

where capital letter denotes the Z-transform of the signal and $H(z)$ is the Z-transform of the Wiener filter h with the transfer function $H(z) = \sum_{i=0}^{N} a_i z^{-i}$, where a_i are constants specific to the filter h. An optimal estimate $\hat{y}$ of the signal of interest y based on the measured signal x is given by

$$\hat{y} = Z^{-1}\{H(z)X(z)\},$$

where $H(z)$ is found by solving the equation

$$\sum_{i=0}^{N} h[i]R_{xx}[t-i] = R_{yx}[t],$$

where $h[i]$ is the impulse response of the filter h, $R_{xx}[t-i]$ is the autocorrelation of x shifted by i time steps and $R_{yx}[t]$ is the cross-correlation between measured signal x and target process y. If the Wiener filter is of zeroth order, this equation simplifies to

$$h[0]R_{xx}[t] = R_{yx}[t]$$
$$\Rightarrow h[0] = \frac{R_{yx}[t]}{R_{xx}[t]} = \frac{C_{yx}}{C_{xx}},$$

and the processed signal is simply

$$\hat{y}[t] = Z^{-1}\{H(z)X(z)\} = h[0]Z^{-1}\{X(z)\} = \frac{C_{yx}}{C_{xx}}x[t].$$

If our target process is the cortical signal in the magnetometer data $\widehat{M_c}$, an estimate can be obtained by Wiener filtering the gradiometer signal G by using M as the target process;

$$\widehat{M_c} = C_{mg}C_{gg}^{-1}G.$$

This Wiener filter of zeroth order simply finds the common temporal subspace between the gradiometers and magnetometers, which represents the cortical component of the magnetometer data, as mentioned above. This cortical component of the magnetometer data can then be removed by an orthogonal projection to this Wiener filter on the raw signal M:

$$\widehat{M_d} = M - \widehat{M_c} = M\left(I - G^T C_{gg}^{-1} G\right),$$

which is exactly our original processing algorithm. CSS is then derived from this expression according to the outline in the "Methods" section. Our method can thus be seen as a tweaked version of an orthogonal projection to a zeroth order Wiener filter using gradiometer data as the corrupted signal and magnetometer data as target process.

CSS Further Explained

Figure 9 shows a graphic illustration of CSS. For a more detailed outline, see the pseudocode presented in Fig. 2 and the "CSS Method Theory" section.

In Detail, How Did We Apply CSS on the ASSR Data?

In summary, CSS was used in the following way on the ASSR data;

1. Average the gradiometer and magnetometer data over epochs
2. Orthonormalize the averaged gradiometer and magnetometer data
3. Cross-correlate the orthonormalized, averaged magnetometer data with the orthonormalized, averaged gradiometer data
4. Singular value decompose (SVD) the cross-correlation matrix
5. Find projection vectors U by multiplying the averaged orthonormalized gradiometer data matrix with the left-sided singular vectors in the SVD of the cross-correlation matrix
6. Pick the top r rows of U, these are the projection vectors to be removed from the magnetometer/EEG data
7. For each epoch, project out the projection vectors from the magnetometer or EEG data

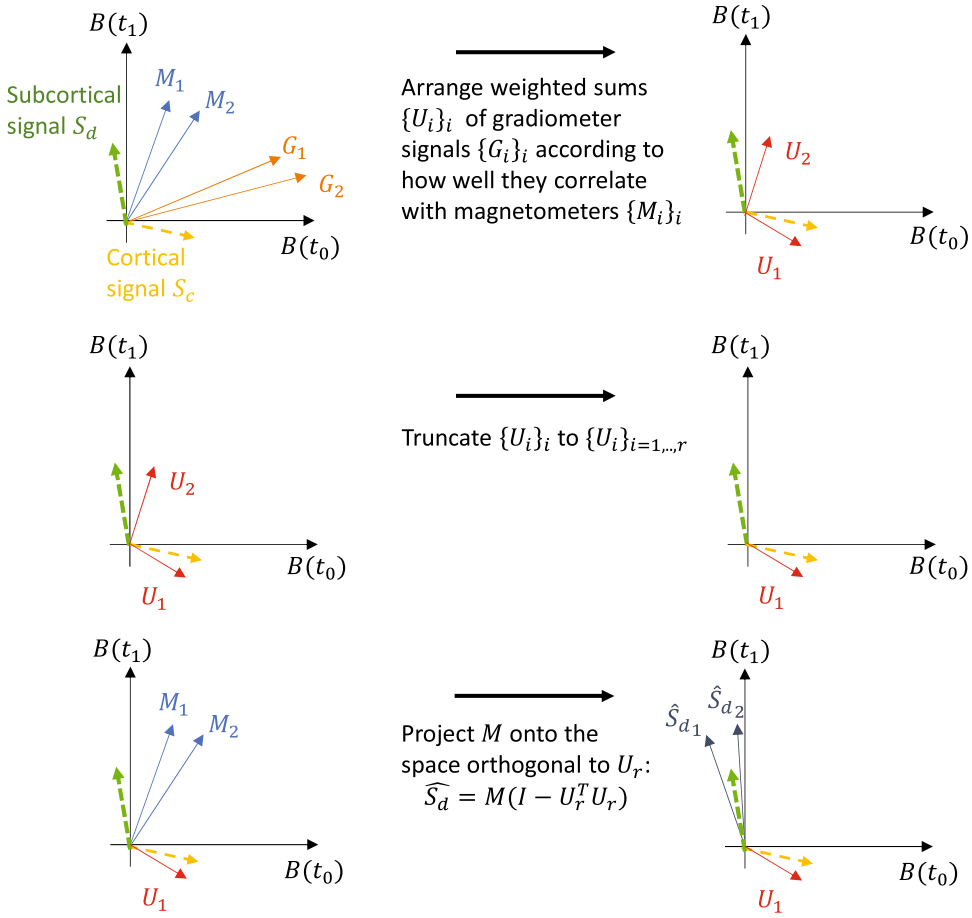

Fig. 9 Illustration of CSS. G_i and M_i are the signals from gradiometer and magnetometer channel i, respectively. The vectors $U_{i=1,\ldots,204}$ are the gradiometer data represented in a new basis, arranged in descending order according to how well they correlate with the magnetometer data. $\widehat{S}_d$ is the estimate of subcortical sensor space signal based on the magnetometer data

References

Ahlfors SP, Han J, Belliveau JW, Hämäläinen MS (2010) Sensitivity of MEG and EEG to source orientation. Brain Topogr 23:227–232. https://doi.org/10.1007/s10548-010-0154-x

Ahonen AI, Hämäläinen MS, Ilmoniemi RJ, Kajola MJ, Knuutila JE, Simola JT, Vilkman VA (1993) Sampling theory for neuromagnetic detector arrays. IEEE Trans Biomed Eng 40:859–869. https://doi.org/10.1109/10.245606

Airaksinen K, Makela JP, Taulu S, Ahonen A, Nurminen J, Schnitzler A, Pekkonen E (2011) Effects of DBS on auditory and somatosensory processing in Parkinson's disease. Hum Brain Mapp 32:1091–1099. https://doi.org/10.1002/hbm.21096

Allen DP, Stegemoller EL, Zadikoff C, Rosenow JM, Mackinnon CD (2010) Suppression of deep brain stimulation artifacts from the electroencephalogram by frequency-domain Hampel filtering. Clin Neurophysiol 121:1227–1232. https://doi.org/10.1016/j.clinph.2010.02.156

Attal Y, Schwartz D (2013) Assessment of subcortical source localization using deep brain activity imaging model with minimum norm operators: a MEG study. PLoS ONE 8:e59856. https://doi.org/10.1371/journal.pone.0059856

Bharadwaj HM, Shinn-Cunningham BG (2014) Rapid acquisition of auditory subcortical steady state responses using multichannel recordings. Clin Neurophysiol 125:1878–1888. https://doi.org/10.1016/j.clinph.2014.01.011

Coffey EB, Herholz SC, Chepesiuk AM, Baillet S, Zatorre RJ (2016) Cortical contributions to the auditory frequency-following response revealed by. MEG Nat Commun 7:11070. https://doi.org/10.1038/ncomms11070

Fitzpatrick JM, Konrad PE, Nickele C, Cetinkaya E, Kao C (2005) Accuracy of customized miniature stereotactic platforms. Stereotact Funct Neurosurg 83:25–31. https://doi.org/10.1159/000085023

Goldenholz DM, Ahlfors SP, Hämäläinen MS, Sharon D, Ishitobi M, Vaina LM, Stufflebeam SM (2009) Mapping the signal-to-noise-ratios of cortical sources in magnetoencephalography and electroencephalography. Hum Brain Mapp 30:1077–1086. https://doi.org/10.1002/hbm.20571

Gramfort A et al (2013) MEG and EEG data analysis with. MNE-Python Front Neurosci 7:267. https://doi.org/10.3389/fnins.2013.00267

Griffiths DJ (2005) Introduction to electrodynamics. Cambridge University Press, Cambridge

Hämäläinen M, Hari R, Ilmoniemi RJ, Knuutila J, Lounasmaa OV (1993) Magnetoencephalography - theory, instrumentation, and applications to noninvasive studies of the working human brain. Rev Mod Phys 65:413–497. https://doi.org/10.1103/RevModPhys.65.413

Hari R, Hämäläinen M, Joutsiniemi SL (1989) Neuromagnetic steady-state responses to auditory stimuli. J Acoust Soc Am 86:1033–1039. https://doi.org/10.1121/1.398093

Hunold A, Funke ME, Eichardt R, Stenroos M, Haueisen J (2016) EEG and MEG: sensitivity to epileptic spike activity as function of source orientation and depth. Physiol Meas 37:1146–1162. https://doi.org/10.1088/0967-3334/37/7/1146

Jiménez-Martínez R, Griffith WC, Knappe S, Kitching J, Prouty M (2012) High-bandwidth optical magnetometer. JOSA B 29(12):3398–3403. https://doi.org/10.1364/JOSAB.29.003398

Jordan C (1875) Essai sur la géométrie à n dimensions. Bull Soc Math France 3:103–174

Knuutila JE et al (1993) A 122-channel whole-cortex SQUID system for measuring the brain's magnetic fields. IEEE Trans Magn 29:3315–3320

Kuwada S, Anderson JS, Batra R, Fitzpatrick DC, Teissier N, D'Angelo WR (2002) Sources of the scalp-recorded amplitude-modulation following response. J Am Acad Audiol 13:188–204

Kwong KK, Belliveau JW, Chesler DA, Goldberg IE, Weisskoff RM, Poncelet BP et al (1992) Dynamic magnetic resonance imaging of human brain activity during primary sensory stimulation. Proc Natl Acad Sci USA 89:5675–5679. https://doi.org/10.1073/pnas.89.12.5675

Lachaux JP, Rodriguez E, Martinerie J, Varela FJ (1999) Measuring phase synchrony in brain signals. Hum Brain Mapp 8:194–208

Malmivuo J, Suihko V, Eskola H (1997) Sensitivity distributions of EEG and MEG measurements. IEEE Trans Biomed Eng 44:196–208. https://doi.org/10.1109/10.554766

Mosher JC, Leahy RM, Lewis PS (1999) EEG and MEG: forward solutions for inverse methods. IEEE Trans Biomed Eng 46:245–259. https://doi.org/10.1109/10.748978

Obeso JA, Concepcio M, Rodriguez-Oroz C, Blesa J, Benitez-Temiño B, Mena-Segovia J et al (2008) The basal ganglia in Parkinson's disease: current concepts and unexplained observations Ann Neurol 64(Suppl 2):S30–S46 https://doi.org/10.1002/ana.21481

Ogawa S, Lee TM, Kay AR, Tank DW (1990) Brain magnetic resonance imaging with contrast dependent on blood oxygenation. Proc Natl Acad Sci USA 87:9868–9872. https://doi.org/10.1073/pnas.87.24.9868

Parkkonen L, Fujiki N, Makela JP (2009) Sources of auditory brainstem responses revisited: contribution by magnetoencephalography. Hum Brain Mapp 30:1772–1782. https://doi.org/10.1002/hbm.20788

Samuelsson J, Tammisola O, Juniper MP (2015) Breaking axi-symmetry in stenotic flow lowers the critical transition Reynolds number. Phys Fluids 27:104103. https://doi.org/10.1063/1.4934530

Taulu S, Hari R (2009) Removal of magnetoencephalographic artifacts with temporal signal-space separation: demonstration with single-trial auditory-evoked responses. Hum Brain Mapp 30:1524–1534. https://doi.org/10.1002/hbm.20627

Uusitalo MA, Ilmoniemi RJ (1997) Signal-space projection method for separating MEG or EEG into components. Med Biol Eng Comput 35:135–140. https://doi.org/10.1007/BF02534144

Vrba J, Fife A, Burbank M, Weinberg H, Brickett P (1982) Spatial discrimination in SQUID gradiometers and 3rd order gradiometer performance Canadian. J Phys 60:1060–1073. https://doi.org/10.1139/p82-144

Wanderah T, Gould D (2016) Nolte's the human brain: an introduction to its functional anatomy, 7th edn. Elsevier, Philadelphia